HOKKAIDO UNIVERSITY

Title	X-Ray Microtomography of Mortars Exposed to Freezing-Thawing Action
Author(s)	Promentilla, Michael Angelo B.; Sugiyama, Takafumi
Citation	Journal of Advanced Concrete Technology, 8(2), 97-111 https://doi.org/10.3151/jact.8.97
Issue Date	2010-07
Doc URL	https://hdl.handle.net/2115/54947
Type	journal article
File Information	X-Ray Microtomography of Mortars Exposed to Freezing-Thawing Action.pdf

Hokkaido University Collection of Scholarly and Academic Papers : HUSCAP

Scientific paper

X-Ray Microtomography of Mortars Exposed to Freezing-Thawing Action

Michael Angelo B. Promentilla[1] and Takafumi Sugiyama[2]

Received 3 February 2010, accepted 15 April 2010

Abstract

This paper presents our findings on the application of X-ray microtomography to characterize the internal structure of mortars that were exposed to freezing-thawing action. A microfocus X-ray CT (micro-CT) scanner was used for the nondestructive 3D imaging of internal air voids or cracks at a spatial resolution of the order of 10 microns. Four different types of mortar specimens (i.e., non-air-entrained and air-entrained Portland cement mortar, and non-air-entrained and air-entrained fly ash mortar) were scanned after being subjected to different numbers of freeze-thaw cycles. Coupled with image analysis, the void space obtained from micro-CT was characterized in three dimensions (3D) in terms of void fraction and air void size distribution, as well as, the crack width and tortuosity of the connected crack network. Results suggest that the initial air voids follow a lognormal distribution with the highest population of modal size around 30-50 μm, irrespective of the type of mortar. As the distributed air voids of non-air entrained mortars were relatively few in numbers, the fly ash mortar in particular was the least resistant against frost damage as shown by the formation of internal cracks that meander around the weaker paste-aggregate interface. Indications also suggest that these cracks are well connected and anisotropic in 3D.

1. Introduction

There are several serious causes of deterioration of concrete structures exposed to various environmental conditions. In particular in cold regions, the freezing-thawing action is among the most significant cause of deterioration. Concrete that is not resistant to cyclic freezing-thawing action manifests two principal types of damage, namely surface scaling and internal cracking (Pigeon *et al*. 1996).

Several methods have been developed to observe and quantify these types of damage caused by freezing-thawing action. For example, the scaling can be easily assessed based on scaled mass loss or visual rating in accordance with ASTM C 672. As for the internal cracks, scanning electron microsopy (SEM) and optical microscopy (OM) have been the most widely used techniques to characterize the cracks in sections of mortar or concrete (Jacobsen *et al*. 1995; Ammouche *et al*. 2001; Elzafraney and Soroushian 2004; Litorowicz 2006). However, the limitations of observing a two-dimensional section of a three-dimensional structure from such 2D microscopy must be borne in mind. In this paper, we used X-ray microtomography to investigate the three-dimensional (3D) microstructure of mortars exposed to freezing-thawing action.

At a spatial resolution of several micrometers, X-ray microtomography is similar in principle to medical computed tomography (CT) scans which create images that map the variation of the X-ray attenuation coefficient within objects. In general, the X-ray beam is radiated to the specimen and the transmitted beam is recorded on a detector. According to Beer-Lambert's law, the ratio of the number of transmitted to incident X-ray photons is related to the integral of the linear attenuation coefficient (LAC) of the material along the path that the photons follow through the specimen. The resulting image (or radiograph) is a superimposed information set or projection of a volume in a 2D plane. Three-dimensional (3D) information is then obtained from radiographic projections of the specimen taken at many angles or projection views. Once these projections are available, a reconstruction algorithm can be used to produce the contiguous two dimensional images which provide a discrete approximation of the distribution of X-ray attenuation coefficient within the volume of the scanned specimen. Since the linear attenuation coefficient (LAC) is a sensitive measure of atomic composition and density, the CT technique could provide a non-invasive and nondestructive 3D visualization and characterization of the internal structures of material (Robb 1982). In other words, X-ray microtomography provides the virtual cross-sectional image without the time-consuming and laborious sectioning of a specimen typically required in 2D microscopy techniques.

Very high-resolution 3D images at a scale of submicron to few microns are nowadays obtained on X-ray CT systems located in synchrotron radiation facilities. At the SPring-8 in Japan, we applied such kind of tech-

[1]Department of Chemical Engineering, College of Engineering, De La Salle University, Manila, Philippines.
E-mail: michael.promentilla@dlsu.edu.ph
[2]Environmental Material Engineering Laboratory, Graduate School of Engineering, Hokkaido University, Japan.

niques to investigate the microstructure of cement pastes (Promentilla *et al*., 2008a, 2009a, 2009b; Sugiyama *et al*., in press). Aside from the high intensity of the X-ray beam from synchrotron radiation as an X-ray source, the parallel and monochromatic beam set-up provide an exact and quantitative reconstruction that is free of beam-hardening artifacts attributed to polychromatic beams (Kinney and Nichols 1992). However, as trade-offs occur between the maximum sample size and the spatial resolution to fit the specimen in the field-of-view of the detector, a synchrotron-based CT system is usually limited to a specimen of millimeter size. On the other hand, for specimens of centimeter size, a cone-beam system can be used with a microfocus X-ray tube as the source that provides a spatial resolution of the order of 10 microns. As this divergent cone-beam of X-rays is polychromatic, several techniques such as the application of filters are being used to reduce the beam-hardening artifacts in the reconstructed image (Van Geet *et al*. 2000).

Despite the fact that microfocus X-ray CT has received considerable attention in materials research including several studies on cement-based materials (e.g., see Salvo *et al*., 2003; De Graef *et al*. 2005; Bentz *et al*. 2006; Naik *et al*. 2006; Elaqra *et al*. 2007), surprisingly little is known on the application of this technique on mortar or concrete specimens exposed to freezing-thawing environments. The purpose of this study is therefore to demonstrate the feasibility of using microfocus X-ray CT to examine and characterize the internal microstructure of frost-induced damaged mortars. This paper focuses on the extraction and quantification of the air void and crack system with the aid of 3D image analysis techniques.

2. Materials and methods

2.1 Sample preparation

Two types of mortar were produced, namely the fly ash mortar and the ordinary Portland cement mortar. The mixture proportions of the mortar specimens used in this experiment are shown in **Table 1**. The cement used was an ordinary Portland cement (OPC) designated as JIS R5210 whereas the fly ash is of JIS type II. The river sand used in the mixture is of sizes that range from 0.15 mm to 2 mm. Chemical admixtures were also added to obtain a desired air content in fresh mortar as measured by the air meter (JIS A1128). For example, an air-entrainment agent with water-reducing effect (AEWR) and an air-entrainment adjustment agent (AEAD) were used in fresh OPC mortar, whereas AEAD alone was found to be effective in introducing sufficient air content in the fly ash mortar. On the other hand, an antifoaming agent (AF) was added to reduce the air content to a reasonable value for the non-air entrained OPC mortar.

In accordance to JIS R5201, the casting in 40 mm x 40 mm x 160 mm steel molds was performed and these molds were stored in a moist condition for 24 hours. The specimens were then cured in water after their removal from the mold. After curing for 14 days, cored cylindrical samples of 12 mm in diameter were obtained from the hardened mortar specimens. From these core samples, cylindrical specimens with aspect ratio (L/D) of 2 were prepared for freezing-thawing experiment and X-ray scanning.

2.2 Freezing-thawing experiment

The specimens were cyclically exposed to freezing in water at -25^{o}C and then thawing in water at 25^{o}C in an air-temperature controlled room. One cycle of the freezing and thawing took about 12 hours. After a specified number of freeze-thaw cycles, the specimens were removed from the controlled room, and then the central portion of each specimen was scanned by microfocus X-ray CT. The relative dynamic modulus of elasticity was also measured indirectly through monitoring the changes of ultrasonic transit time in the axial direction of the cylindrical specimen with a PUNDIT (Portable ultrasonic non-destructive digital indicating tester) device.

2.3 Image acquisition using microfocus X-ray CT

Acquisition of 3D images of the internal structure of specimens subjected to cyclic freezing-thawing envi-

Table 1 Mixture proportions of the test specimens[a].

Specimens [b]	FA %	W/B %	Unit weight (kg/m^3)							Air[c] (%)
			W	C	S	FA	AEWR	AEAD	AF	
P-NA	0	50	281	562	1405	0	0	0	0.0086	1.3
F-NA	30	50	274	384	1372	165	0	0	0	0.2
P-AE	0	50	271	542	1355	0	1.63	0.16	0	7.2
F-AE	30	50	265	371	1324	159	0	0.5	0	7.8

[a] NOTE: FA = Fly ash, W=Water, C=Cement, S=Sand, AEWR=Air-entrainment agent with water reducing effect, AEAD=Air-entrainment adjustment agent, AF = Anti-foaming agent.
[b] non-air-entrained OPC mortar (P-NA), non-air-entrained fly ash mortar (F-NA), air-entrained OPC mortar (P-AE), air-entrained fly ash mortar (F-AE)
[c] initial air content of fresh mortar from air meter measurement (Pressure method).

ronment was done using a desktop microfocus CT system (TOSCANER-30000μhd, Toshiba IT & Control Systems Corporation, Japan). The microfocus X-ray CT (micro-CT) scanner (see **Fig. 1**) consists of a microfocus X-ray source, a specimen manipulator, an image intensifier (II) detector coupled to a CCD camera, and an image processing unit (Promentilla *et al*. 2008b). A power setting of 130 kV and 124 μA was used for a full (360°rotation) cone-beam scan with 1500 projection views. The specimen was set in a holder mounted on a precision rotation table, and then the table position was adjusted to fit the image within the field-of-view. Scanning parameters and conditions were adjusted to obtain high resolution images, as well as to reduce the noise and artifacts in the images during acquisition. The image acquisition time for each specimen that includes both scanning and reconstruction time was about one and a half hours. Further image processing and analysis were also done using public domain programs such as ImageJ (Rasband 2007) and SLICE (Nakano *et al* 2006).

3. Results and discussion

3.1 Pre-processing of CT data from cone-beam scanning

The data set obtained from cone-beam scanning of the central portion of the specimen (about 12-mm and 8-mm in diameter and height, respectively) consists of contiguous 199 slices of reconstructed CT images with thickness of 40 micron each (**Fig. 2**). Stacking up these slices creates a 3D image of the scanned section of the specimen. Each slice is a grayscale image having a matrix size of 1024 x 1024 pixels with an in-plane resolution (x-y plane) of 12 μm/pixel. Accordingly, each voxel (volume element or volumetric pixel) in the raw CT data has anisotropic dimensions of 12 x 12 x 40 μm. Each voxel is also associated with a raw CT number (CTN) that is proportional to the average X-ray attenuation coefficient of the material in the said voxel. Since the attenuation coefficient depends on the atomic composition and density, the voxels associated with low-density phases such as air or water have much lower CT number as compared with that of the solid matrix of the mortar. In grayscale images, the lower CT number is typically shown as a darker intensity level than that of the higher CT number.

For example, **Fig. 3** shows a representative slice of the specimen after rescaling the raw 14-bit (16384 intensity levels) CT data to an 8-bit (256 intensity levels) grayscale image. As shown in the histogram of the CT number (**Fig. 3a**), there are two distinct peaks which are associated with the air and the solid matrix, respectively. From the raw CT data, different brightness and contrast of the converted image can be obtained by adjusting the Window Level (WL) and Width (WW) as shown in **Figs. 3c** and **3d**. Such data conversion defined by WL and WW is depicted in **Fig. 3b**. In this study, all the CT data were consistently converted to 8-bit grayscale images (e.g., TIF images) by setting the WL and WW to 400 and 700, respectively. In other words, we defined 50

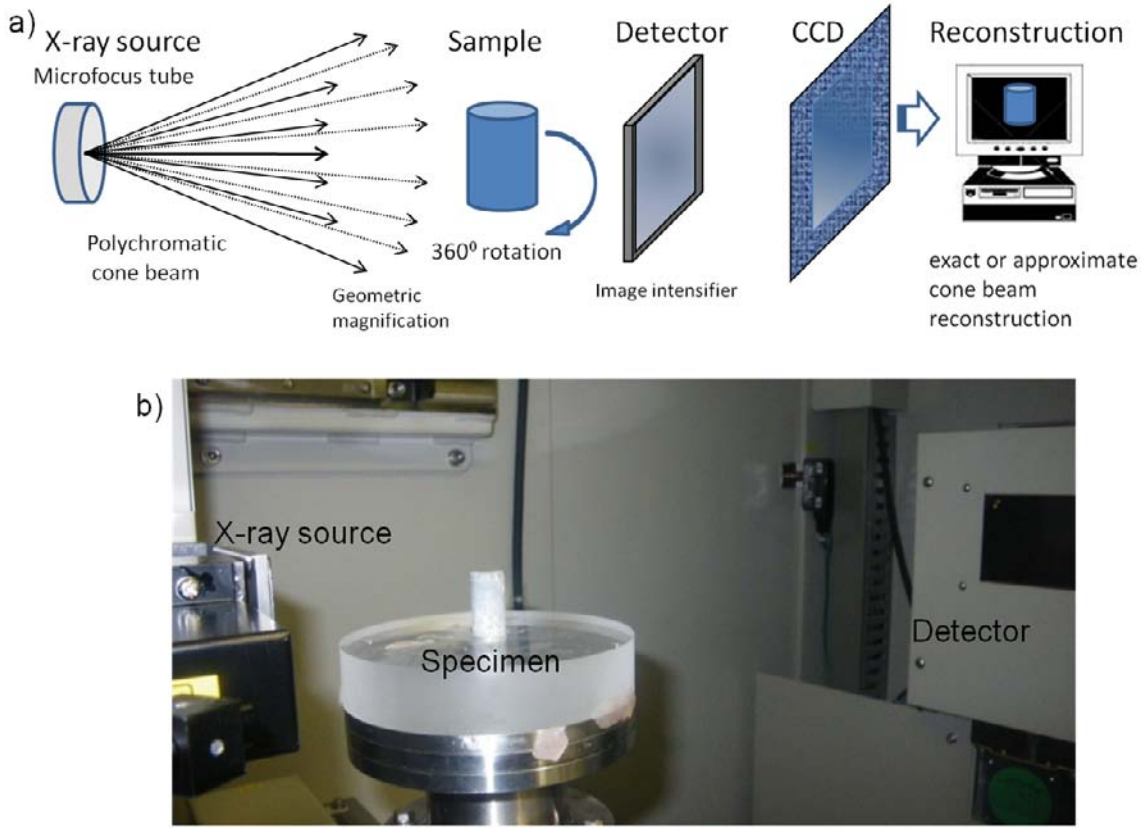


Fig. 1 Experimental setup of the microfocus X-ray CT.

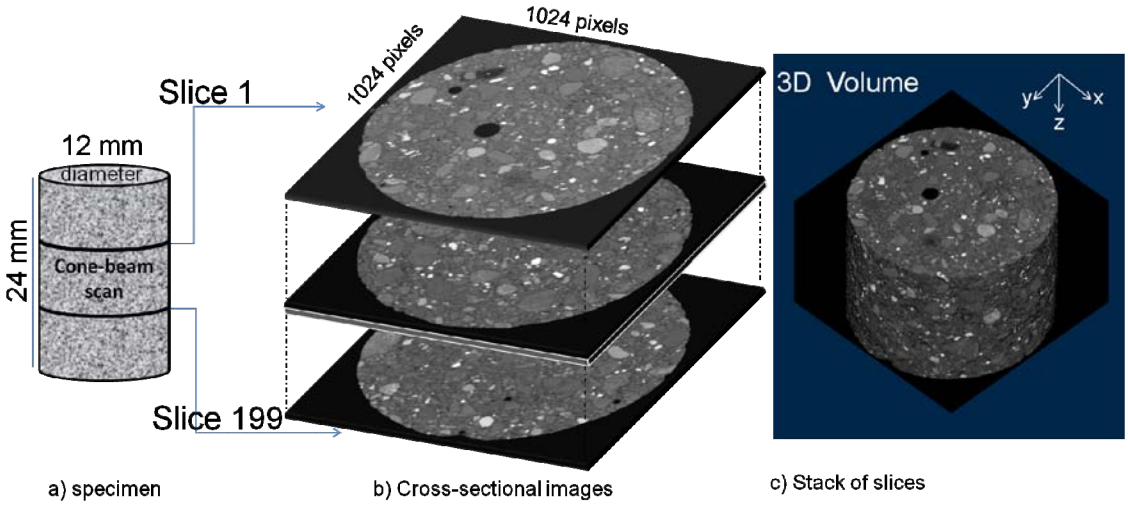


Fig. 2 CT data from the scanned section of the specimen.

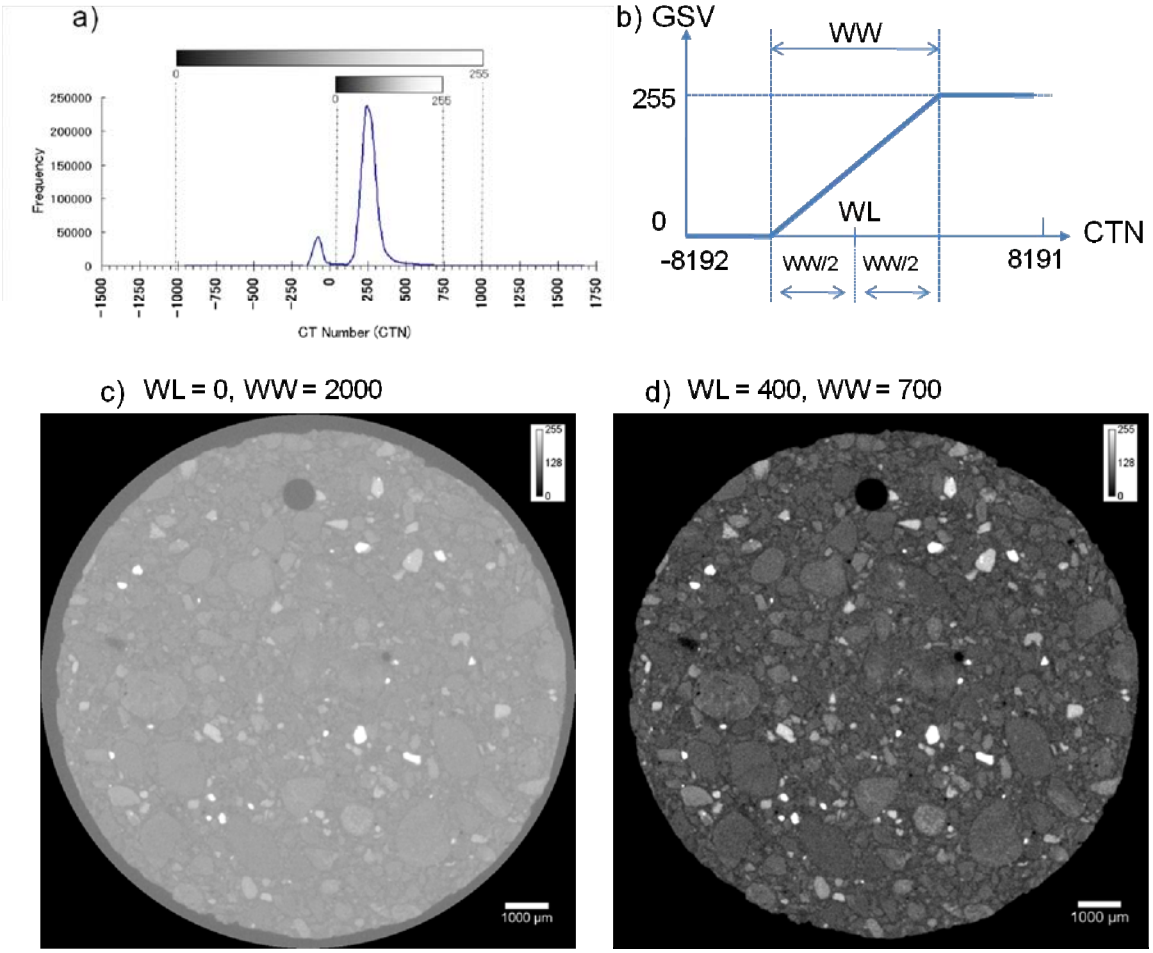


Fig. 3 CT histogram of the reconstructed image of a cross-section of the specimen (F-NA) and the corresponding displayed 8-bit grayscale images of different brightness and contrast.

(i.e., WL – WW/2) and 750 (i.e., WL + WW/2) as the minimum and maximum CTN cut-off, respectively to give a better contrast between the surrounding air and the mortar matrix. Hence, any voxel with CTN less than or equal to 50 was transformed to a grayscale value (GSV) of zero (black) whereas any voxel with more than 750 was transformed to a GSV of 255 (white). For voxels with CTN between 50 and 750, the following equation was used in scaling the CTN to 8-bit (0-255) grayscale image: GSV = (255/700) (CTN – 50).

Denoising based on the anisotropic diffusion filter was also applied to the stack of 8-bit grayscale images. The anisotropic diffusion filter has been demonstrated effective in removing noise while preserving the edges (e.g., see Sheppard *et al*., 2004). **Figure 4** shows an example of the resulting slice including the respective histogram and line profile before and after the denoising process.

3.2 Microtomographic images of specimen subjected to freezing-thawing cycle

Figures 5-8 illustrate the sample cross-sectional images of the specimens at different number of freeze-thaw (FT) cycles. For example, the slice 40, 100, and 160 represent the upper, middle, and bottom part of the scanned sections. In these figures, the aggregates (sand particles) were imaged as patches of various shades of gray, and appeared to be brighter relative to darker shades of gray of the surrounding cement paste. On the other hand, the air voids and cracks were clearly seen as black or very dark voxels in the microtomographic images. Most of the cracks meander around the aggregates suggesting that these cracks attempt to follow the weaker interfacial transition zone (ITZ) between the

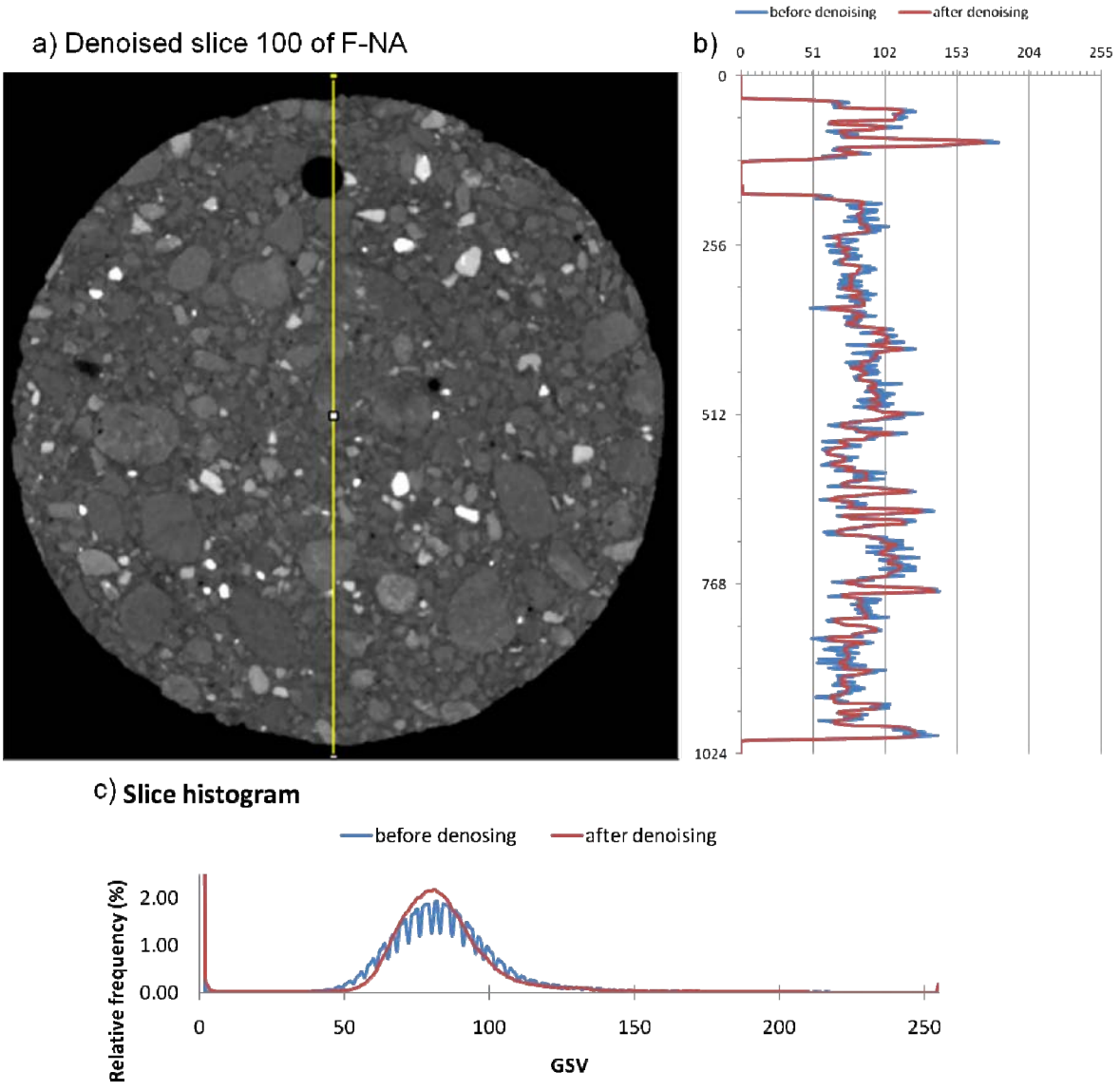


Fig. 4 Sample denoised image with line profile and slice histogram of that CT image before and after denoising.

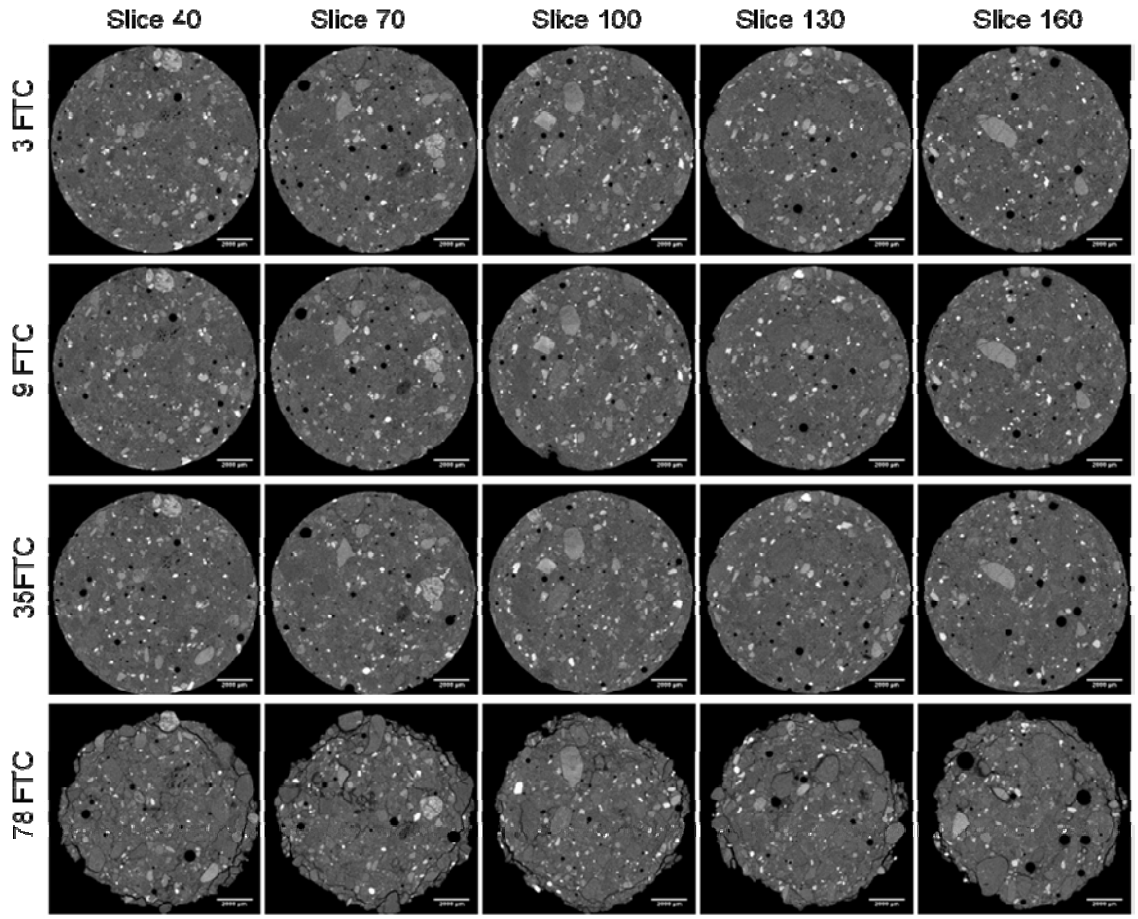


Fig. 5 Sample cross-sections of non-air-entrained OPC mortar (P-NA) at different freeze-thaw cycles (FTC).

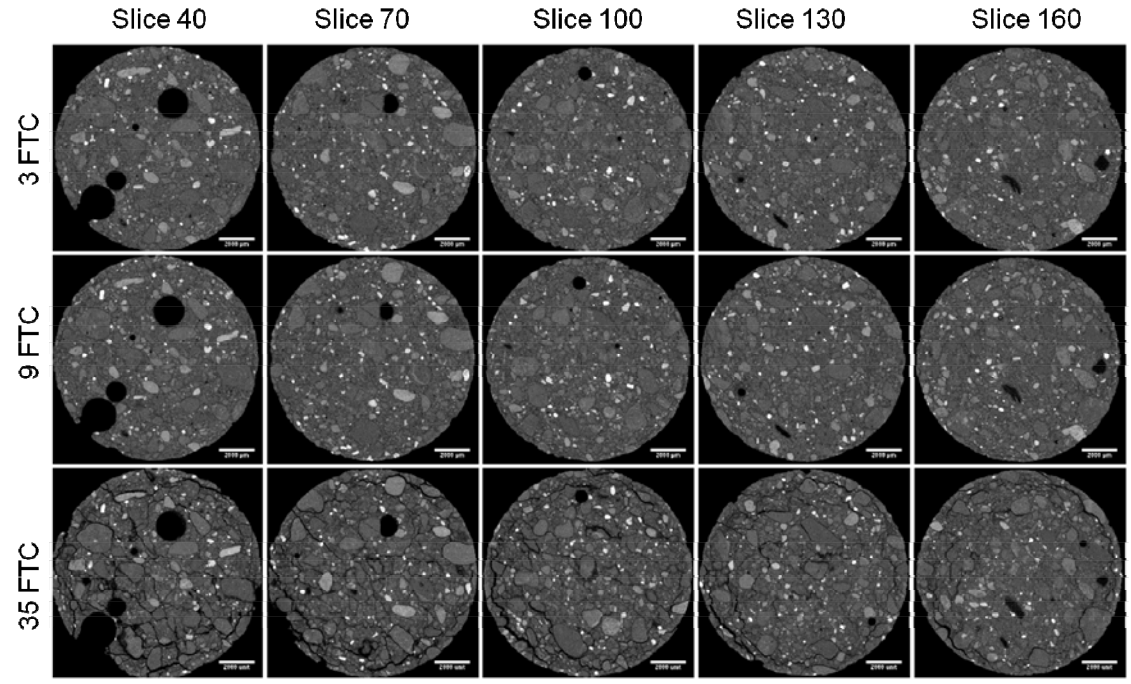


Fig. 6 Sample cross-sections of non-air-entrained fly ash mortar (F-NA) at different freeze-thaw cycles (FTC).

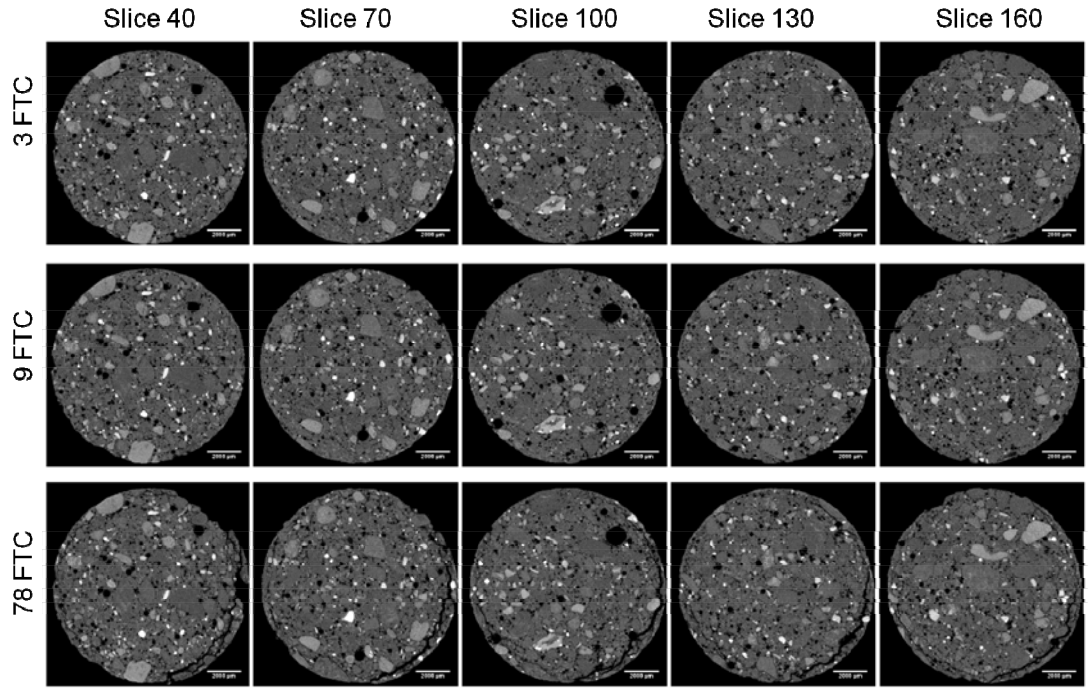


Fig. 7 Sample cross-sections of air-entrained OPC mortar (P-AE) at different freeze-thaw cycles (FTC).

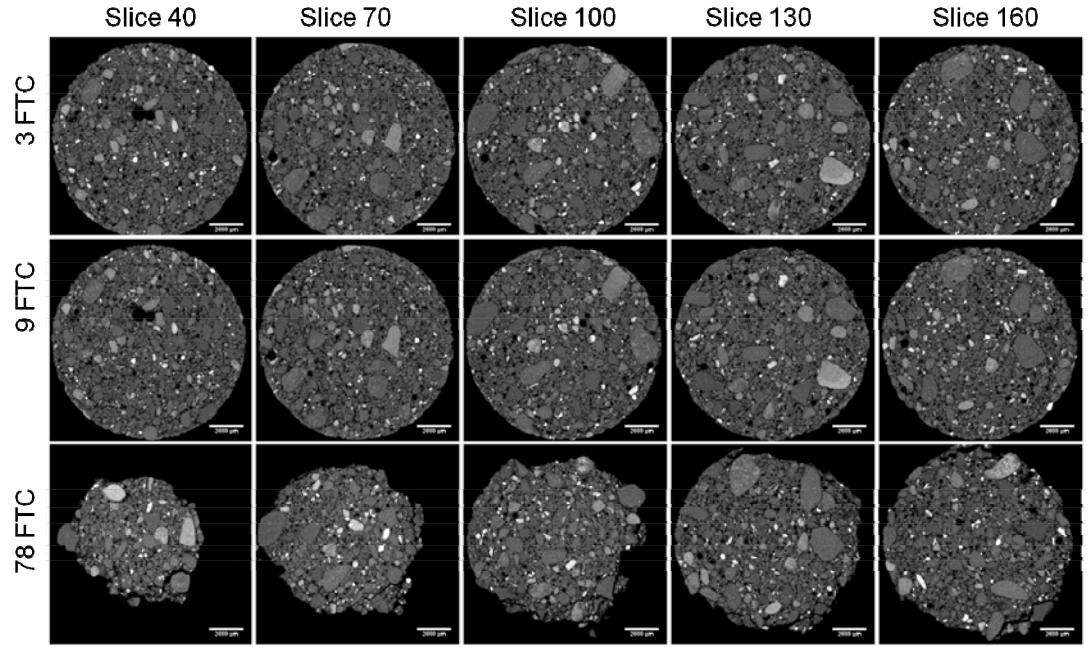


Fig. 8 Sample cross-sections of air-entrained fly ash mortar (F-AE) at different freeze-thaw cycles (FTC).

sand and the cement paste in the frost-induced damaged mortars.

At 3 FT cycles for all specimens, only air voids were clearly visible as indicated by the various sizes of circular dark regions distributed in the cross-sections. As expected, the non-air-entrained mortars (P-NA and F-NA) exhibited internal damage after a number of FT cycles as shown by the cracks formed throughout the cross-section (see **Figs 5-6**). At 35 FT cycles, surface and internal cracks are clearly seen in non-air-entrained fly ash mortar (F-NA) as compared to that of non-air-entrained OPC mortar (P-NA). This suggests that the rate of internal deterioration for F-NA appeared to be greater than that of P-NA. This finding was also supported by the results obtained from the relatively rapid decline of the relative dynamic modulus of elasticity

(RDME) for F-NA through a number of FT cycles as shown in **Fig. 9**. The RDME values were computed from the square of the ratio of the measured ultrasonic pulse velocity at a given number of FT cycles to that of the initial condition (i.e., at 0 FTC). Note that the RDME of F-NA and F-AE were measured only until 19 and 34 FT cycles, respectively because of the failure of the instrument to monitor the ultrasonic transit time in the specimens. The excessive scaling at the surface of the said specimens where the PUNDIT transducers were being placed prevented us to measure properly the ultrasonic time.

As for the CT images of air-entrained mortars (P-AE and F-AE), no internal cracks were observed but some cracks near the radial surface were found at 78 FT cycles. These surface cracks may serve as the precursor of frost scaling. Interestingly, the dramatic change of the cross-sectional area of the foreground image in F-AE suggests significant scaling in this specimen (see **Fig. 8**). This preliminary finding seems to be consistent with some of the previously reported studies (Thomas 1997) but warrants further investigation in the future.

3.3 Extraction and quantification of void space from microtomographic images

To visualize and quantify the air voids or cracks, a number of image analysis routines was applied to the CT images. First, the void space (air void or crack) was extracted from the images through global thresholding (see **Fig. 10**). Since a gray scale value (GSV) of zero was assumed to be associated with air, the grayscale threshold value was selected as one half of the GSV of the peak associated with the solid matrix as shown in **Fig. 10a**. In other words, the threshold value used was the average value of the GSV most likely associated with the said two phases. Based from the visual inspection of the CT images, this threshold value was found to be adequate for this study. Thus, any voxels with GSV below or equal to this threshold value are considered void space and assigned a value of zero (shown as black in **Fig. 10c**). Otherwise, any voxels with GSV above this threshold value are considered as solid and assigned a value of 255 (shown as white in **Fig. 10c**). This simple image segmentation technique produces the binary images (black and white) that separate the void space from the solid matrix (see **Fig. 10c**). However, additional image operations (see **Figs. 10d-f**) were needed to be done to separate the surrounding air from the interior void space. The resulting images (e.g., see **Fig. 10f**) were then used to further analyze the internal void space (black voxels) only. For example, the void fraction was easily quantified by dividing the total number of internal void voxels (e.g., black in **Fig. 10f**) with the total number of foreground voxels (e.g., black in **Fig. 10e**).

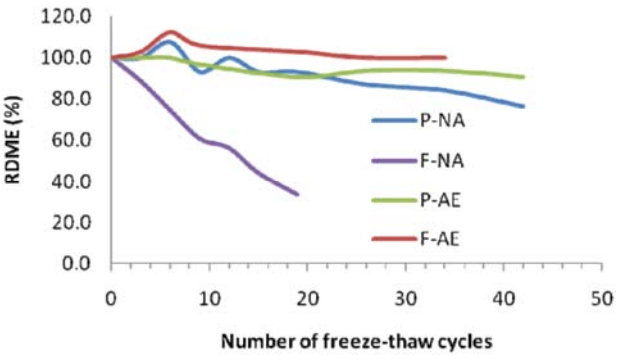


Fig. 9 Relative dynamic modulus of elasticity (RDME) of the specimens as the cyclic freezing and thawing progresses.

Figure 11 summarizes the void fraction of the scanned specimen at different number of FT cycles. Since we did not see any clear cracks at 3 FT cycles, it was assumed that the computed void fraction at 3 FT cycles approximates the initial air content of the scanned specimen. An increase in the void fraction after a number of FT cycles would indicate the formation of frost-induced cracks throughout the specimen. It is therefore not surprising that F-NA had the most significant increase of void fraction (i.e., a steeper slope in **Fig. 11**) as shown by the clear formation of internal cracks in the microtomographic images.

3.4 Characterization of the air void system

Aside from the initial air content obtained from image analysis, we also determined the air void distribution from the 3D images at 3 FTC. Connectivity analysis through a multiple cluster labeling technique (Hoshen and Kopelman 1976; Ikeda *et al*. 2000) was performed to identify, label and measure the volume and surface area of the individual void objects (or clusters). A void cluster is defined as the group of void voxels that are connected to each other by sharing a common face. Prior to connectivity analysis, the stack of 3D images was rescaled along the z-axis using cubic spline interpolation to create an isotropic voxel of 12 μm. Moreover, morphologic binary operations such as opening and watershed algorithm were also applied to separate overlapping air voids as much as possible before determining the void size distribution (Promentilla *et al*. 2008c; Vincent and Soille 1991).

Figure 12 describes the void size distribution obtained from the analysis of the CT images including the visualization of the air voids in three dimensions. Note that the equivalent diameters were calculated from the estimated volume of each cluster, i.e., the individual isolated air voids. Assuming the air void follows a more or less spherical shape, the equivalent diameter refers to the diameter of a sphere having the same volume as that of the void. These equivalent void diameters were classified in a 10-μm class interval frequency histogram.

Although the study is limited in its extent, results from the histogram suggest that the air void system follows a log-normal distribution with a modal size around 30 to 50 μm for both non-air-entrained and air-entrained mortars. In contrast to that of non-air-entrained mortar, the addition of air entrainment obviously increases the

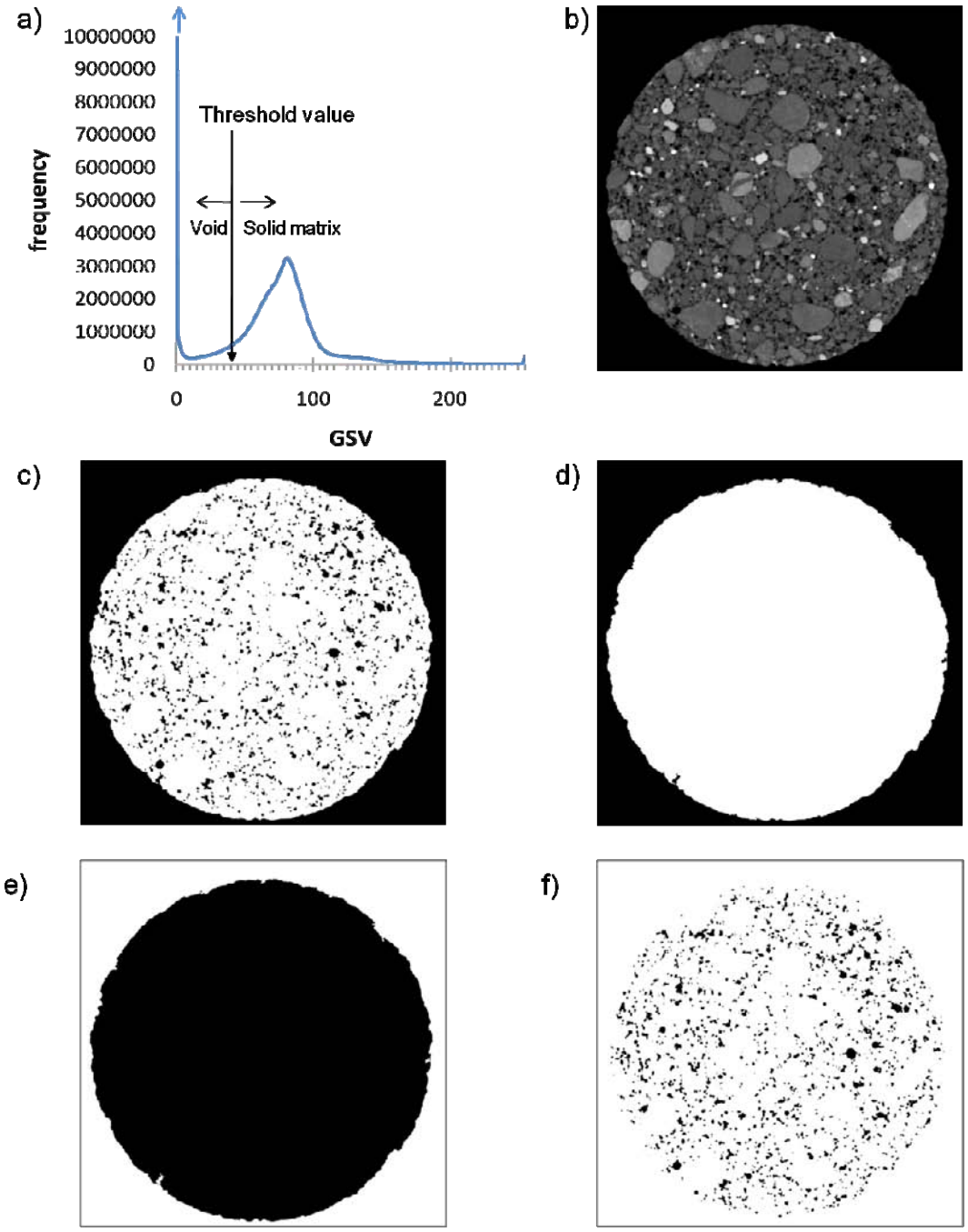


Fig. 10 Extraction of void space from the CT images. a) stack histogram of the CT images of specimen (F-AE) including the threshold value for void segmentation, b) 8-bit grayscale image of sample slice or cross-section, c) binary image of b) after thresholding, d) binary image of c) after fill-hole operation, e) invert image of d), and f) image addition of c) and e).

number of air voids in air-entrained mortars in the size range between 20 and 200 μm. Thus, air-entrained mortars would be expected to have higher values of void number density and total specific surface of air voids, and in effect a better void spacing to protect the interior cement paste from frost damage (Promentilla *et al* 2008c, Sugiyama *et al*. 2008). This is consistent with the findings obtained from this study. The non-air-entrained fly ash mortar (F-NA) exhibited the least resistance to frost damage as indicated by the formation of the 3D crack network that was clearly seen by the micro-CT.

3.5 Characterization of the crack system

Table 2 summarizes the results of connectivity analysis of the void space of F-NA at different FT cycles. Indica-

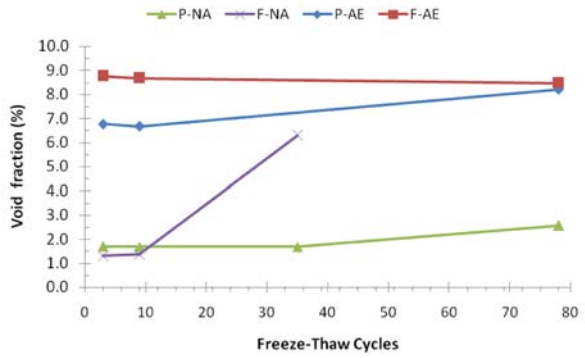


Fig. 11 Estimated void fraction at different freeze-thaw (FT) cycles.

tion was found to suggest that not only the formation of internal cracks had caused the increase of the total volume and surface area of the void space, but also the degree of void connectivity. This void connectivity was estimated from the ratio of the volume of largest void cluster to that of the total void space. The degree of connectivity would therefore be one if all the air voids and cracks are connected to each other to form only one large void cluster. The cracks may not be seen as connected in 2D cross-sectional images but the 3D information provided by microtomography allows us to evaluate the degree of connectivity of these cracks. The dramatic increase of void connectivity at 35 FT cycles indicates that the individual cracks form a well-connected crack system in three dimensions. For example, this crack network was about 82 % of the total void space extracted from the CT images of F-NA.

Furthermore, the 3D medial axis (3DMA) analysis (Lindquist *et al*. 1996; Lindquist 1999; Prodanovic *et al*. 2006) or skeletonization algorithm was used to measure some geometric parameters of this crack network in three dimensions. The medial axis transform of the digitized void space, often referred to as a 'skeleton', refers to a simplified representation of the original 3D data in which important information about the topology and geometry of the original structure is maintained. The modified burning algorithm of Lee *et al* (1994) (Lindquist *et al*. 1996) was used to identify the set of medial axis voxels, each with a unique burn number, which is related to its distance from the closest solid voxel.

For the purpose of illustration, a cubic volume of interest (VOI, L = 6 mm) was selected to analyze the internal crack system (see **Fig. 13**). Note that the crack network from this VOI is percolating in three directions such that the cracks are connected to the six faces of the said VOI. Volume rendering of this percolating crack space is shown in **Fig. 13c**. From this 3D image, the medial axis transform was applied to obtain the skeleton of the crack network, i.e., the set of medial axis voxels with associated burn number. The burn number can then

Table 2 Summary of the void multiple cluster labeling analysis of F-NA.

Parameters (F-NA)	FTC = 3	FTC = 9	FTC = 35
No. of clusters	28419	33334	68134
Total volume (mm^3)	11.1	11.5	53.9
Total surface area (mm^2)	268.5	324.6	3438.4
Volume of the largest cluster (mm^3)	3.8	3.8	44.1
Degree of connectivity	0.34	0.33	0.82

be used to roughly estimate the voxel-wise width of crack, which may be about twice the associated burn number less one voxel. For example, about 95 % of the medial axis voxels of the crack system have burn numbers of less than 2 as shown in **Fig. 14**. This indicates a crack width distribution with the highest population of width that ranges between 36 (3-voxels wide) to 48 (4-voxels wide) microns.

In addition, path tortuosity (e.g. see **Fig. 15a**) was also evaluated according to the connectivity of the cracks between two parallel faces of the VOI. Geometric path tortuosity (τ) was defined as the ratio of the actual path length to the shortest distance along the x, y, or z-directions. This dimensionless parameter, which is equal or greater than one, indicates the degree of winding of the crack. Quantification of such parameter is found to be useful in modeling the effect of cracking on transport properties of damaged cement-based materials (Gerard and Marchand 2000; Ringot and Bascoul 2001). In contrast to 2D microscopy, we could therefore take advantage of the 3D information provided by micro-CT to measure crack tortuosity. As shown in **Fig. 15b**, the average path tortuosity in x and y direction was almost the same, and was slightly lower than that of the z-direction. This may suggest the slight anisotropy of crack network in 3D wherein the extent of internal damage of the cylindrical specimen in the radial direction is not the same as that of the damage in longitudinal (or axial) direction. However, it is also possible that the measured anisotropy may be an artifact attributed to the differences between the in-plane resolution (pixel size of 12 μm) and the out-plane resolution (slice thickness of 40 μm) of the CT images. Further study would therefore be needed to clarify the crack anisotropy obtained from these CT images.

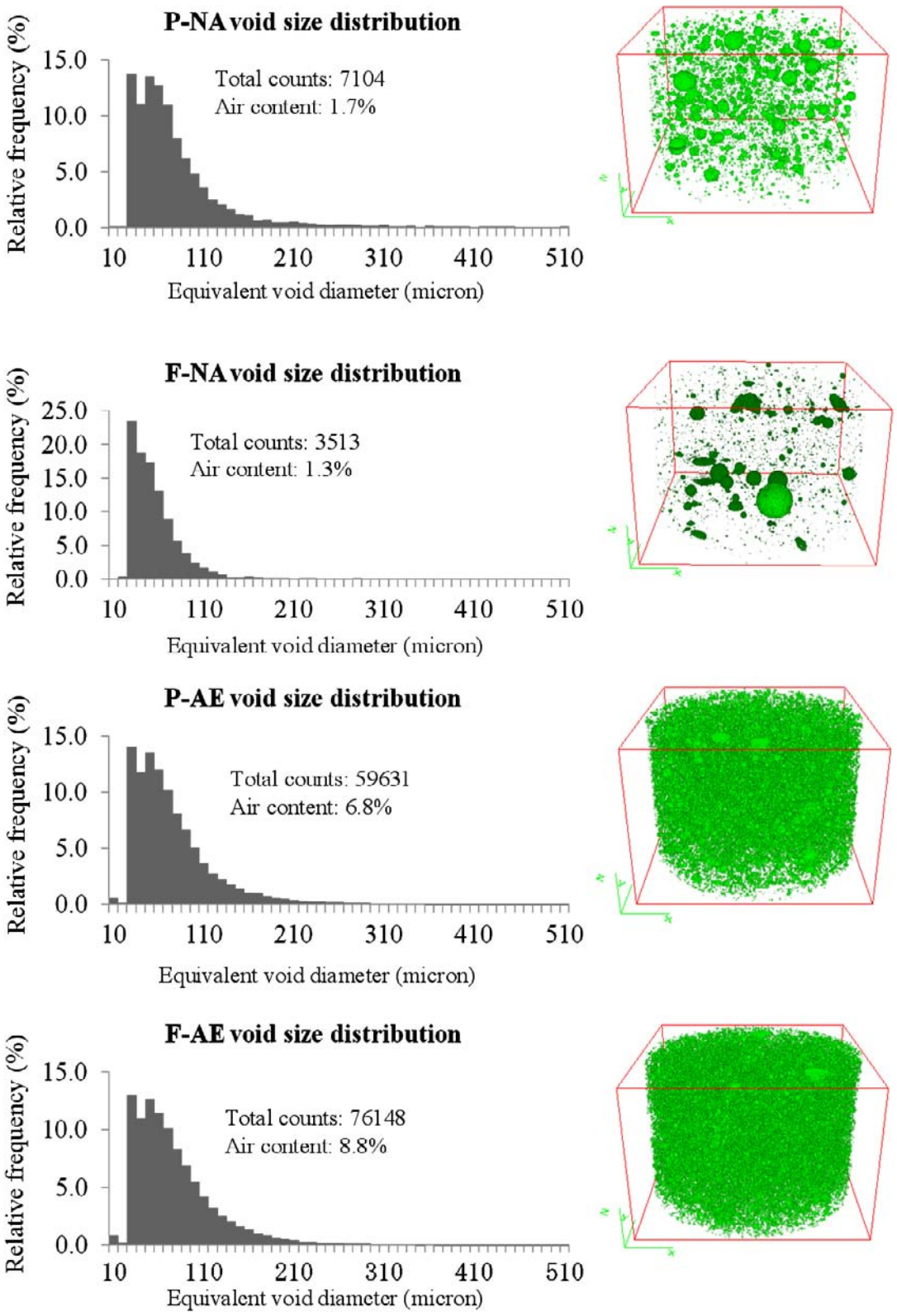
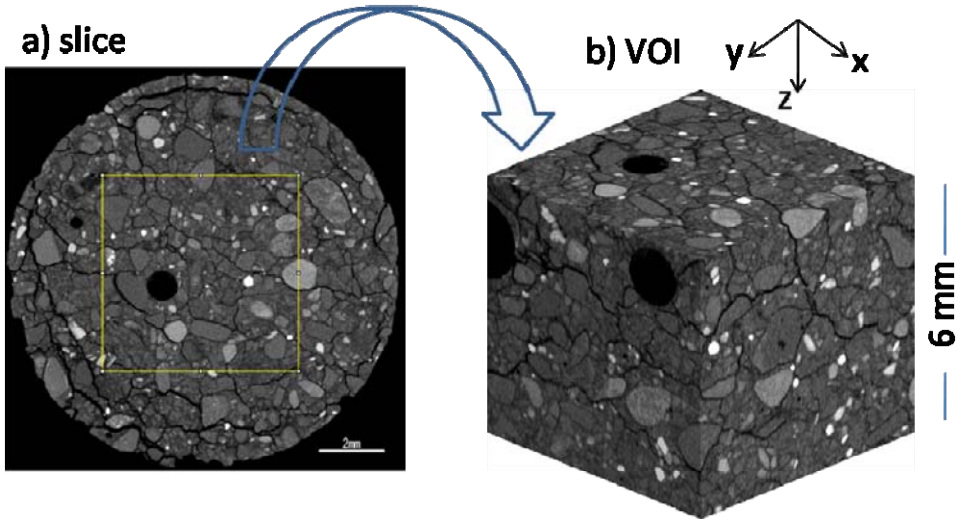


Fig. 12 Initial air content and void size distribution of the specimens.



c) Rendered volume of percolating crack network at different 3D views

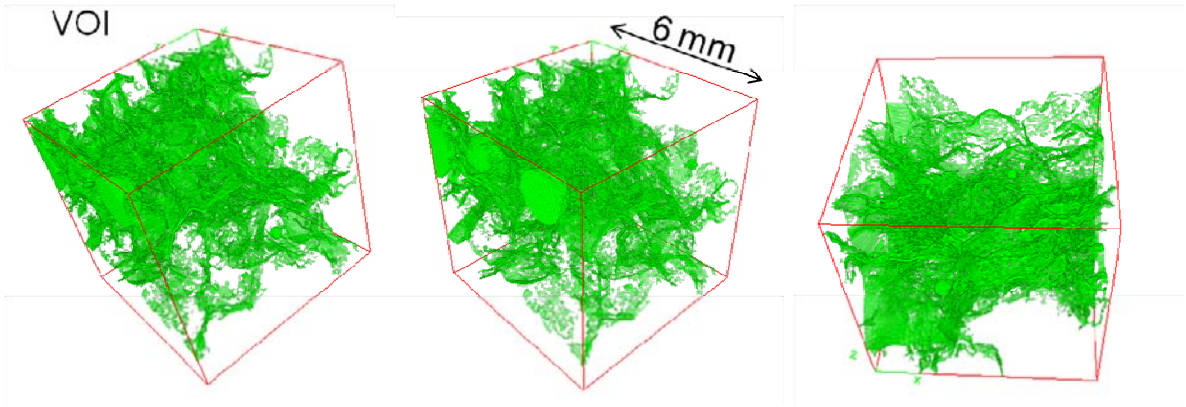


Fig. 13 Volume of interest (VOI) for the 3D medial axis analysis of the percolating internal crack formed in non-air-entrained fly ash mortar.

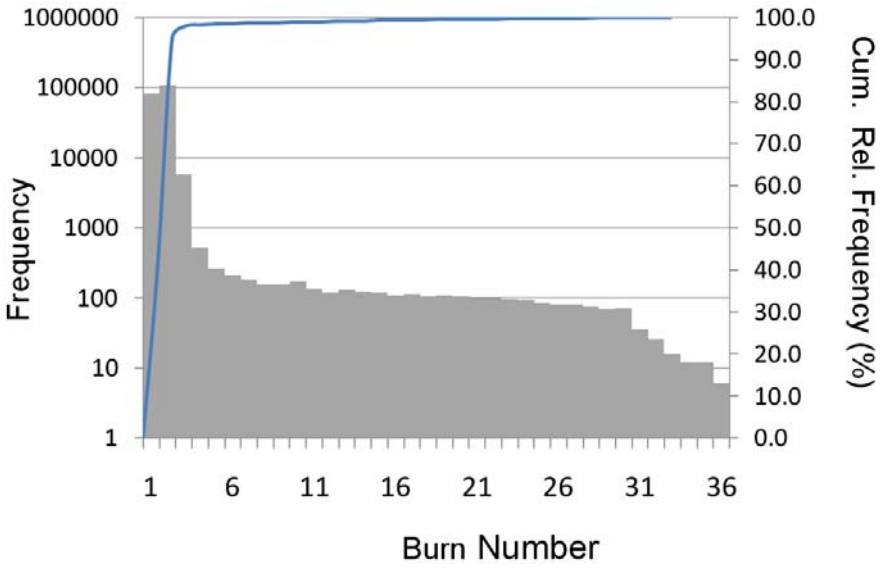


Fig. 14 The burn number distribution of medial axis associated with the crack network in VOI.

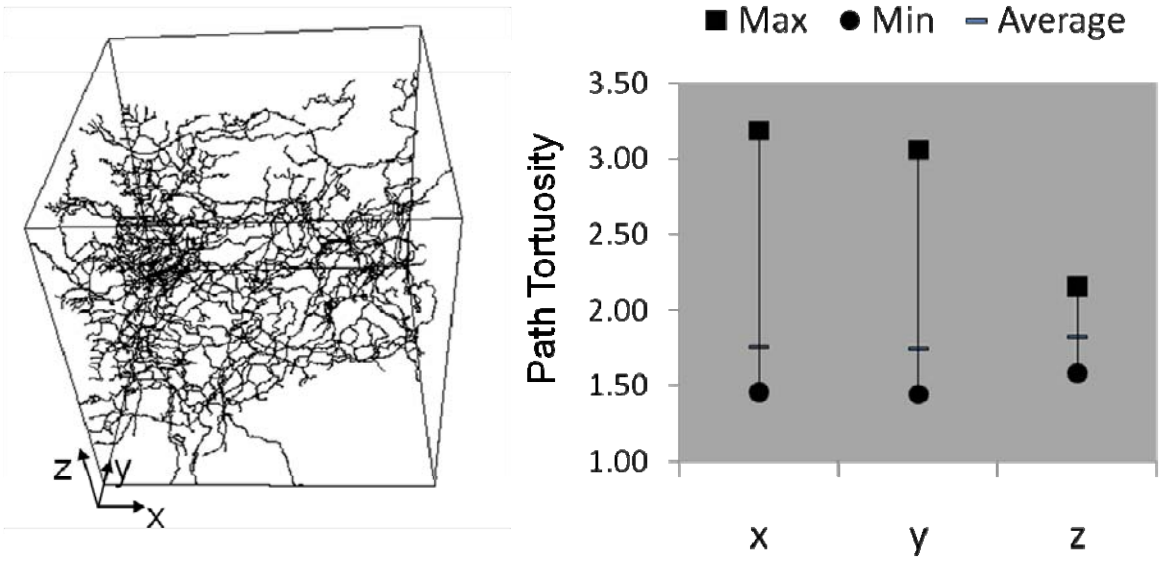


Fig. 15 Geometric path tortuosity of the crack system in three orthogonal directions of VOI.

4. Conclusion

This study demonstrates the promising potential of microfocus X-ray CT (micro-CT) as a noninvasive and nondestructive imaging technique to investigate the microstructure of mortars exposed to freezing-thawing action. The micro-CT coupled with 3D image analysis allows us to visualize and quantify air voids and cracks in the mortar specimen at a spatial resolution on the order of 10-μm order. Although the addition of air entrainment obviously increases the number of air voids in air-entrained mortars in the size range between 20 and 200 μm, our findings suggest that the initial air void size distribution follows a log-normal distribution with a modal size around 30 to 50 microns for both OPC and fly ash mortar, with or without air entrainment. With inadequate void spacing to protect the interior cement paste in non-air entrained mortars, significant cracks were observed relatively earlier, for example, in non-air entrained fly ash mortar after a number of freeze-thaw (FT) cycles. In addition, measurement of void fraction including the volume, surface area, and degree of connectivity of void space in three dimensions allows us to gain useful insight on the damage evolution caused by frost action. Further characterization of the 3D crack network also suggests crack anisotropy, as well as a crack width distribution that is largely populated by widths of less than 50 microns. Quantifying such 3D crack parameters could lead to a better understanding and modeling of the relationship of crack formation and the changes of the material properties during deterioration. As technology in image acquisition, processing, analysis and computational methods continually improve, we could therefore take advantage of the 3D information provided by X-ray microtomography, not only to visualize, but also to quantity more accurately the air void and cracks parameters and to assess the durability performance of cement-based materials against freezing-thawing action. Moreover, the application of this proposed method could be extended to study other cracks associated with various deterioration mechanisms.

Acknowledgments

The authors are grateful to the three anonymous reviewers for their valuable suggestions and insights in improving the content of this paper. Part of this research is funded by Research Grant from the Japan Society for the Promotion of Science (Kiban kenkyu B, Sugiyama, T. Research No.19360193). The authors would like to thank Prof. Kaneko and Dr. Kawasaki for allowing them to use the micro-CT scanner and also to Mr. Hatakeda and Dr. Shimura for his assistance in the preparation of the specimen. The first author also acknowledges the postdoctoral fellowship support from the Japan Society for the Promotion of Science.

References

Ammouche, A., Riss, J., Breysse, D. and Marchand, J. (2001). "Image analysis for the automated study of microcracks in concrete." *Cement and Concrete Composites*, 23, 267–278.

Bentz, D. P., Halleck, P. M., Grader, A. S. and Roberts, J. W. (2006). "Four-dimensional X-ray microtomography study of water movement during internal curing." In: Jensen, O.M., Lura, P. and Kovler, K. Eds., *Proceedings of the International RILEM Conference - Volume Changes of Hardening*

Concrete: Testing and Mitigation, RILEM Publications S.A.R.L., 11-20.

De Graef, B., Cnudde, V., Dick, J., De Belie, N., Jacobs, P. and Verstraete, W. (2005). "A sensitivity study for the visualization of bacterial weathering of concrete and stone with computerized X-ray microtomography." *Science of the Total Environment*, 341, 173-183.

Elaqra, H., Godin, N., Peix, G., Mili, M. R. and Fantozzi, G. (2007). "Damage evolution analysis in mortar, during compressive loading using acoustic emission and X-ray tomography: effects of the sand/cement ratio." *Cement and Concrete Research.* 37(5), 703-713.

Elzafraney, M. and Soroushian, P. (2004). "Assessment of microcrack development in concrete materials of different strengths." *Materials and Structures*, 274, 724-731.

Gérard, B. and Marchand, J. (2000). "Influence of cracking on the diffusion properties of cement-based materials. Part I: Influence of continuous cracks on the steady-state regime." *Cement Concrete Research,* 30, 37-43.

Hoshen, J. and Kopelman, R. (1976). "Percolation and cluster distribution. I. Cluster multiple labeling technique and critical concentration algorithm." *Phys. Rev. B.* 14, 34-38.

Ikeda, S., Nakano, N. and Nakashima, Y. (2000). "Three-dimensional study on the interconnection and shape of crystals in a graphic granite by X-ray CT and image analysis." *Mineralogical Magazine.* 64(5), 945-959.

Jacobsen, S., Marchand, J. and Hornain, H. (1995). "SEM observations of the microstructure of frost deteriorated and self healed concrete." *Cement and Concrete Research*, 25(8), 55-62.

Kinney, J.H. and Nichols, M. C. (1992). "X-ray tomographic microscopy using synchrotron radiation." *Ann. Rev. Materials Sci* 22. 121-152.

Lee T-C., Kashyap, R. and Chu C-N. (1994). "Building skeleton models via 3-d medial surface/axis thinning algorithms." *CVGIP Graph Models Image Process* 56, 462-478.

Lindquist, W. D., Lee, S.-M., Coker, D., Jones, K. and Spanne, P. (1996). "Medial axis analysis of three-dimensional tomographic images of drill core samples." *Journal of Geophysical Research*, 101B, 8297-8310.

Lindquist, W. D. (1999). "*3DMA General Users Manual*." New York: State of New York at Stony Brook.

Litorowicz, A. (2006). "Identification and quantification of cracks in concrete by optical fluorescent microscopy." *Cement and Concrete Research*, 36, 1508-1515.

Naik, N. N., Jupe, A. C., Stock, S. R., Wilkinson, A. P., Lee, P. L. and Kurtis, K. E. (2006). "Sulfate attack monitored by microCT and EDXRD: Influence of cement type, water-to-cement ratio, and aggregate." *Cement and Concrete Research*, 36, 144-159.

Nakano, T., Tsuchiyama, A., Uesugi, K., Uesugi, M. and Shinohara, K. (2006). "*SLICE -Software for basic 3-D image analysis* [online]." Japan Synchrotron Radiation Research Institute (JASRI). Available from: http://www-bl20.spring8.or.jp/slice/ [5 April 2007].

Pigeon, M., Marchand, J. and Pleau, R. (1996). "Frost resistant concrete." *Construction and Building Materials*, 10(5), 339-348.

Prodanovic, M., Lindquist, W. B. and Seright, R. S. (2006). "Porous structure and fluid partitioning in polyethylene cores from 3D X-ray microtomographic imaging." *Journal of Colloid and Interface Science*, 298, 282-297.

Promentilla, M. A. B., Sugiyama, T., Hitomi, T. and Takeda, N. (2008a). "Characterizing the 3D pore structure of hardened cement paste with synchrotron microtomography." *Journal of Advanced Concrete Technology*, 6(2), 273-286.

Promentilla, M. A. B., Sugiyama, T. and Shimura, K. (2008b). "Three-dimensional imaging of cement-based materials with X-ray tomographic microscopy: Visualization and quantification." In: *Proceedings of the International Conference on Microstructure-related Durability of Cementitious Concrete*, Nanjing: China, 13-15 Oct. 2008. 1357-1366.

Promentilla, M. A. B., Sugiyama, T. and Shimura, K. (2008c). "Three dimensional characterization of air void system in cement-based materials." In: *Proceedings of the 3rd Asian Concrete Federation (ACF) International Conference*, Ho Chi Minh: Vietnam,11-13 Nov. 2008. 940-947.

Promentilla, M. A. B., Sugiyama, T., Hitomi, T. and Takeda, N. (2009a). "Quantification of tortuosity in hardened cement pastes using synchrotron-based X-ray computed microtomography." *Cement and Concrete Research*, 39, 548-557.

Promentilla, M. A. B., Sugiyama, T., Hitomi, T. and Takeda, N. (2009b). "Pore space analysis and estimation of transport properties of deteriorated cementitious material using synchrotron microtomography." In: *Proceedings of the 2nd International RILEM workshop on Concrete Durability and Service Life Planning (ConcreteLife 2009)*. Haifa: Israel. 7-9 Sept. 2009. 498 - 506.

Rasband, W. (2007). *ImageJ: Image processing and analysis in Java*, National Institute of Health (NIH). Available from: http://rsb.info.nih.gov/ij/.

Robb, R. (1982). "X-ray computed microtomography: From basic principles to applications." *Ann. Rev. Biophys. Bioeng,* Annual Reviews Inc. 11:177-201.

Ringot, E. and Bascoul, A. (2001). "About the analysis of microcracking in concrete." *Cement Concrete and Composites*, 23, 261-266.

Salvo, L., Cloetens, P., Maire, E., Zabler, S., Blandin, J. J., Buffière, J. Y., Ludwig, W., Boller, E., Bellet, D. and Josserond, C. (2003). "X-ray micro-tomography

an attractive characterisation technique in material science." *Nucl Instrum Methods Phys Res* B200, 273-286.

Sheppard, A. P., Sok, R. M. and Averdunk, H. (2004). "Techniques for image enhancement and segmentation of tomographic images of porous materials." *Physica A*, 339 (1-2), 45-151.

Sugiyama, T., Promentilla, M. A. B., Shimura, K. and Hatakeda, D. (2008). "Observation of entrained air distribution in mortar by X-ray computed tomography." In: *Proceedings of the Concrete Structure Scenarios, JSMS*, 8, 99-104 (in Japanese).

Sugiyama, T., Promentilla, M. A. B., Hitomi, T. and Takeda, N. (2010). "Application of synchrotron microtomography for pore structure characterization of deteriorated cementitious materials due to leaching." *Cement and Concrete Research,* in press.

Thomas, M. D. A., (1997). "Laboratory and field studies of salt scaling in fly ash concrete." In: *Frost Resistance of Concrete, Proceedings of the RILEM International Workshop on Resistance of Concrete to Freezing and Thawing with or without De-icing Chemicals*, 21-30.

Van Geet, M., Swennen, R. and Wevers, M. (2000). "Quantitative analysis of reservoir rocks by microfocus X-ray computerised tomography." *Sediment. Geol.* 132, 25-36.

Vincent, L. and Soille, P. (1991). "Watersheds in digital spaces: An efficient algorithm based on immersion simulations." *IEEE Transactions on Pattern Analysis and Machine Intelligence.* 13, 583-585.